REPORT

THERMOELECTRICS

High-entropy-stabilized chalcogenides with high thermoelectric performance

Binbin Jiang[1]*, Yong Yu[1,2]*, Juan Cui[1]*, Xixi Liu[1], Lin Xie[1], Jincheng Liao[3], Qihao Zhang[3], Yi Huang[1], Shoucong Ning[2], Baohai Jia[1], Bin Zhu[1], Shengqiang Bai[3], Lidong Chen[3], Stephen J. Pennycook[2], Jiaqing He[1,4]†

Thermoelectric technology generates electricity from waste heat, but one bottleneck for wider use is the performance of thermoelectric materials. Manipulating the configurational entropy of a material by introducing different atomic species can tune phase composition and extend the performance optimization space. We enhanced the figure of merit (*zT*) value to 1.8 at 900 kelvin in an n-type PbSe-based high-entropy material formed by entropy-driven structural stabilization. The largely distorted lattices in this high-entropy system caused unusual shear strains, which provided strong phonon scattering to largely lower lattice thermal conductivity. The thermoelectric conversion efficiency was 12.3% at temperature difference ΔT = 507 kelvin, for the fabricated segmented module based on this n-type high-entropy material. Our demonstration provides a paradigm to improve thermoelectric performance for high-entropy thermoelectric materials through entropy engineering.

Conversion processes waste more than two-thirds of the energy in the world, which can be potentially collected by technology that captures waste heat (*1*). Thermoelectric technology is an attractive option because it can be easily adopted for many situations as a result of its small size and lack of rotating parts or gas emissions (*2*, *3*). One major obstacle to using thermoelectric technology for real applications is the low conversion efficiency. The efficiency is directly determined by the dimensionless figure of merit [$zT = S^2\sigma T/(\kappa_e+\kappa_L)$] of thermoelectric materials (*4*, *5*), where S, σ, T, κ_e, and κ_L are the Seebeck coefficient, electrical conductivity, absolute temperature, carrier thermal conductivity, and lattice thermal conductivity, respectively. All of these parameters can be optimized by tuning band structures, microstructures, and bond states with a range of proposed strategies such as band convergence (*6*), resonant level (*7*), alloying (*2*), nanostructure (*8*), anharmonicity (*4*), and liquid-like ions (*9*). Although these efforts are named with different physical terminologies, the general strategy is to improve electrical transport properties and destroy the thermal transport path. In general, high-entropy alloys (HEAs) should provide a good way to improve thermoelectric performance by strengthening phonon scattering because of their disorder and distorted lattice. Manipulating the electronic properties to maintain electron transport can then be accomplished by trying to use the wide range of chemical compositions to vary phase composition and band structure (*10*).

HEAs are typically defined as a solid solution with more than five principal elements, each in a 5 to 35% molar ratio (*11*) (Fig. 1A). This concept has been extended into creating entropy-stabilized functional materials (*10*). The first reported entropy-stabilized high-entropy functional material was (Mg,Co,Ni,Cu,Zn)O oxide (*12*), which was followed by perovskites, fluorite, spinels, carbides, and silicides (*10*). For a given system, the configurational entropy will increase with increasing element species, leading to the decreased Gibbs free energy and stabilized crystal structure when the increase of entropy is larger than that of enthalpy (*10*, *12*). The change of energy manifests as the extended solubility limits of alloying elements or the entropy-driven structural stabilization effect (*13*, *14*). More accurately, a new phase formed by using entropy as the driving force, contributing to the extended phase space for performance optimization. The stabilized structure can keep

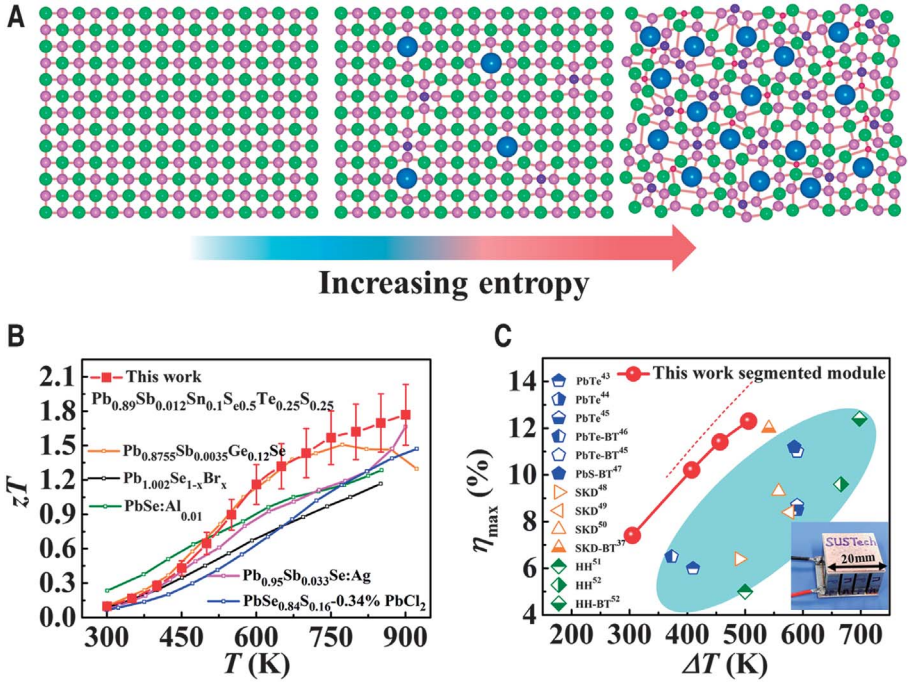

Fig. 1. Improving the performance of thermoelectric materials and modules through entropy engineering. (**A**) Diagram of lattice distortion with increasing entropy. The pink, red, green, blue, and purple spheres represent Pb, Sn, Se, Te, and S atoms, respectively. (**B**) *zT* values as a function of temperature for the high-entropy n-type PbSe-based materials in this work. Some reported *zT* values for traditional n-type PbSe-based materials are also included for comparison (*38*–*42*). (**C**) Maximum conversion efficiencies (η_{max}) as a function of temperature difference (ΔT) for the high-entropy segmented thermoelectric module in this work and some reported results from the literature, as indicated by the superscript [PbTe, skutterudites (SKD), and half-Heusler (HH)] (*37*, *43*–*52*). The red dashed line denotes the simulated values, the blue-shaded area indicates the previously reported results, and the inset is a photograph of the fabricated thermoelectric module.

[1]Shenzhen Key Laboratory of Thermoelectric Materials, Department of Physics, Southern University of Science and Technology, Shenzhen 518055, China. [2]Department of Materials Science and Engineering, National University of Singapore, Singapore 117575, Singapore. [3]State Key Laboratory of High Performance Ceramics and Superfine Microstructure, Shanghai Institute of Ceramics, Chinese Academy of Sciences, Shanghai 200050, China. [4]Guangdong-Hong Kong-Macao Joint Laboratory for Photonic-Thermal-Electrical Energy Materials and Devices, Southern University of Science and Technology, Shenzhen 518055, China.
*These authors contributed equally to this work.
†Corresponding author. Email: hejq@sustech.edu.cn

the long-range order of atomic arrangement, thereby maintaining the electrical transport framework. Meanwhile, short-range disorder in high-entropy materials exists because of the severe lattice distortion from the mismatch of ionic mass, size, and bond state (*15*). The distorted lattice strongly scatters heat-carrying phonons and largely lowers the lattice thermal conductivity of high-entropy materials (*16*, *17*), yielding low thermal transport properties to keep the temperature difference in the thermoelectric module.

Enhanced thermoelectric performance has been reported in $(Cu/Ag)_8Ge(Se/Te)_6$, (Cu/Ag)(In/Ga)Te_2, and (Sn/Ge/Pb/Mn)Te high-entropy materials (*14*, *18*–*20*). Though the thermoelectric performance was enhanced by increasing the configurational entropy in these materials, we have a poor understanding about the relationship between configurational entropy, microstructure, and thermoelectric properties. This is because microstructural investigations are usually focused on dislocations and nanoprecipitates rather than the high-entropy matrix. Additionally, the previous high-entropy thermoelectric materials may actually have been stabilized because of the negative formation enthalpy, with compositions within the solubility limit. We increased the configurational entropy by alloying Sn to form a cubic phase of n-type high-entropy (Pb/Sn)(Se/Te/S) materials over the solubility limit. This may prove to be an effective strategy for developing high-entropy thermoelectric systems using the entropy-driven structural stabilization effect. The manipulated entropy contributed to an ultrahigh zT value of 1.8 at 900 K in an n-type $Pb_{0.89}Sb_{0.012}Sn_{0.1}Se_{0.5}Te_{0.25}S_{0.25}$ high-entropy material (Fig. 1B). The optimized thermoelectric performance translated to an exceptionally high conversion efficiency of 12.3% at ΔT = 507 K in the fabricated segmented thermoelectric module (Fig. 1C), which is notable for the temperature range.

Solubility in alloys is limited by the size and mass differences between solute and solvent atoms, making it challenging to realize high-entropy alloys by increasing alloying content (*10*, *21*). When the contents of S and Te were each less than 0.2, we determined, using x-ray diffraction (XRD) patterns, that the samples had single-phase rock-salt structure (Fig. 2). Increasing S and Te content to 0.25 resulted in the (200) peak splitting into several peaks, which we attributed to multiple phases with different fractions of S, Se, and Te. We used energy dispersive spectroscopy (EDS) mapping (fig. S3) to verify that we formed separate phases rather than a phase transition to lower symmetry. Introducing Sn into the alloy results in the split peaks converging into a single (200) peak, which displayed a typical structural stabilization effect. We calculated the configurational entropy, enthalpy, and Gibbs free energy (Fig. 2B) and found that the structural stabilization effect could be well explained by the competition between entropy and enthalpy. The dependence of the Gibbs free energy (ΔG) on enthalpy (ΔH) and entropy (ΔS) is defined as $\Delta G = \Delta H - T\Delta S$. We calculated ΔH using density functional theory (DFT) and ΔS by the following equation (*22*):

$$\Delta S = -R\left[\left(\sum_{i=1}^{N} x_i \ln x_i\right)_{\text{cation}} + \left(\sum_{j=1}^{M} x_j \ln x_j\right)_{\text{anion}}\right] + \Delta S_{\text{vib}}$$

where R, N, M, x_i, and x_j are the gas constant, atomic species at the cation and anion sites, and the alloyed contents, respectively. We calculated the vibrational entropy (ΔS_{vib}) using DFT (fig. S2). Our calculated curves of the entropy, enthalpy, and Gibbs free energy clearly showed that the Pb(Se/Te/S) system should separate into the multiphase mixture with high S and Te content because of enthalpy-driven phase separation. With the introduction of another element Sn, the increase in entropy is faster than that of enthalpy, resulting in entropy-driven structural stabilization and the high-entropy range with a negative Gibbs free energy. The translation from the multiphase mixture to single phase through increasing configurational entropy in the (Pb/Sn)(Se/S/Te) system clearly shows that the entropy-driven structural stabilization effect can be an effective strategy for forming different high-entropy materials whose composition is over the solubility limit. The benefit of seeking out materials with compositions over the solubility limit is that it provides a more varied range that may be helpful for optimizing performance.

To further verify our single-phase identification in $Pb_{0.89}Sb_{0.012}Sn_{0.1}Se_{0.5}Te_{0.25}S_{0.25}$ (Fig. 2A and fig. S1), we also conducted high-angle annular dark field (HAADF) and atomic x-ray EDS analysis using scanning transmission electron microscopy (STEM) at different scales and in different areas (Fig. 2, C to H, and figs. S4 and S5) to investigate the homogeneity of this material. We found that the distribution of all elements was homogeneous from the micrometer to nanometer scales. Moreover, in

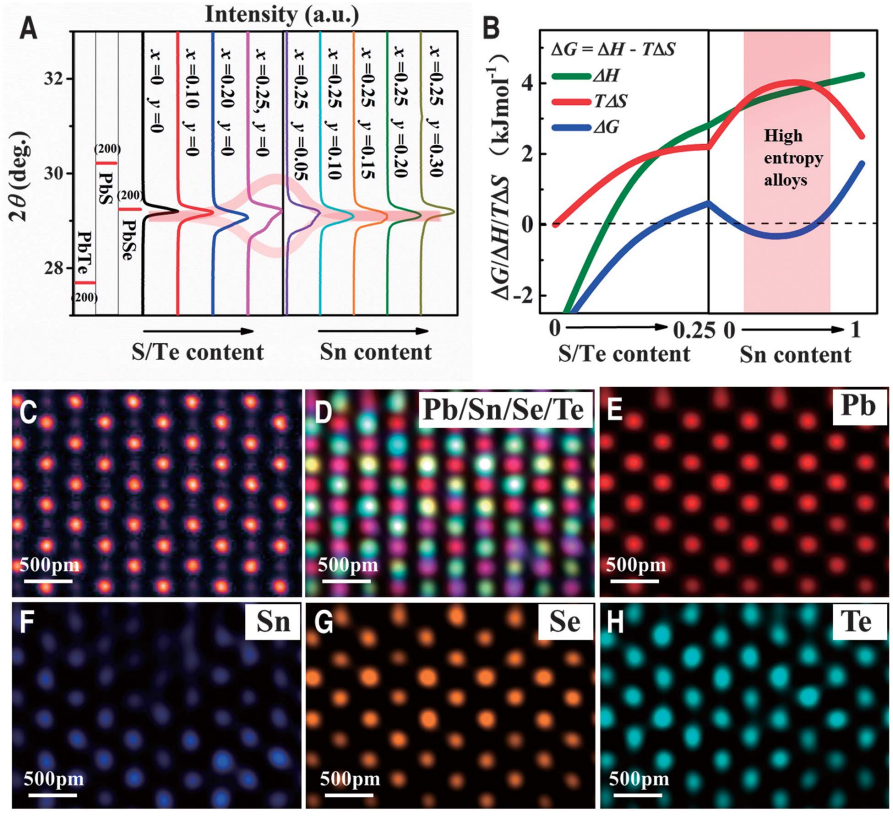

Fig. 2. Stabilizing single-phase structure by increasing the entropy. (**A**) XRD patterns of PbSe-based materials with increasing S/Te and Sn content ($Pb_{0.99-y}Sb_{0.012}Sn_ySe_{1-2x}Te_xS_x$, where x changes from 0 to 0.25 and y changes from 0 to 0.3). The red-shaded area indicates entropy-stabilized high-entropy composition. a.u., arbitrary units. (**B**) Entropy, enthalpy, and Gibbs free energy as a function of S/Te and Sn content. (**C** to **H**) Shown are a (C) HAADF image along the [110] zone axis; (D) Pb, Sn, Se, and Te total EDS mapping; and (E) Pb, (F) Sn, (G) Se, and (H) Te partial EDS mapping of a high-entropy $Pb_{0.89}Sb_{0.012}Sn_{0.1}Se_{0.5}Te_{0.25}S_{0.25}$ sample. S element mapping is not shown because of the weak signal and the overlapped peak with Pb, as shown in fig. S6.

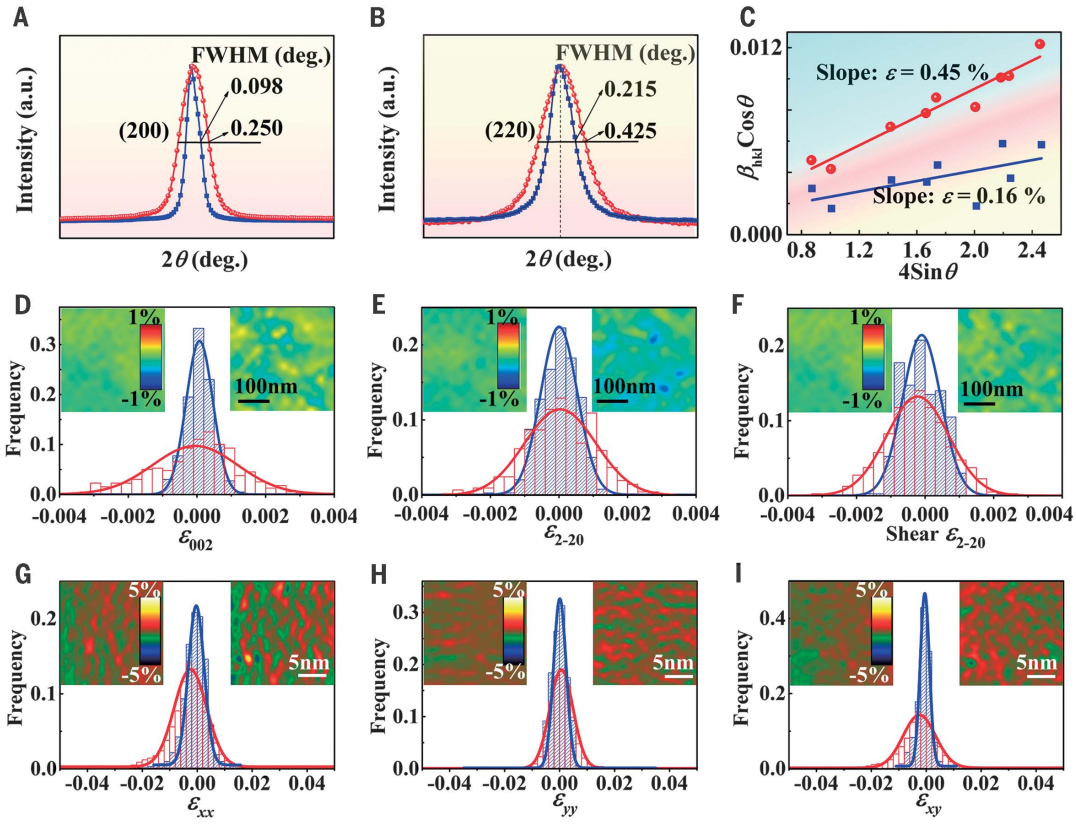

Fig. 3. Strain analysis at different scales. (**A** and **B**) Enlarged (A) (200) and (B) (220) peaks of powder XRD results for a high-entropy $Pb_{0.89}Sb_{0.012}Sn_{0.1}Se_{0.5}Te_{0.25}S_{0.25}$ sample (red). A traditional low-entropy $Pb_{0.99}Sb_{0.012}Se$ sample (blue) is also included for comparison. (**C**) Calculated lattice strains (ε) based on Williamson-Hall analysis. Statistical and spatial distribution of normal and shear strains measured by NBED and GPA. Red and blue represent the same samples as defined in (A) and (B). β_{hkl}, the FWHM of the (hkl) peak. (**D** to **I**) Normal strains along the (D) (002) and (E) (2-20) directions and shear strains along the (F) (2-20) direction based on NBED results are shown. Normal strains along the (G) *xx* and (H) *yy* directions and shear strains along the (I) *xy* direction based on GPA results are shown. The blue lines and left insets are from a low-entropy $Pb_{0.99}Sb_{0.012}Se$ sample. The red lines and right insets are from a high-entropy $Pb_{0.89}Sb_{0.012}Sn_{0.1}Se_{0.5}Te_{0.25}S_{0.25}$ sample.

the ultrahigh-resolution EDS mappings (Fig. 2, D to H), the atomic lattices and positions of every element were very clear, demonstrating that the atomic arrangement order stabilized by increasing entropy even though many atom species were introduced into one structure. The homogeneous distribution of the five elements across all scales distinguishes a high-entropy material from low-entropy and multiphase materials. The well-defined atomic arrangement is distinct from amorphous materials.

The entropy-driven stabilization allowed for a well-maintained atomic arrangement, but the strong mismatch of atomic size severely distorted the lattice and should strongly affect the thermal transport process (*13*, *16*, *17*). To visualize the distorted lattice, we measured the strains of low-entropy ($Pb_{0.99}Sb_{0.012}Se$) and high-entropy ($Pb_{0.89}Sb_{0.012}Sn_{0.1}Se_{0.5}Te_{0.25}S_{0.25}$) samples at different scales (Fig. 3). The broadened peaks [the (200) peak in Fig. 3A and the (220) peak in Fig. 3B] in our XRD data clearly demonstrate the increased strains from these distorted lattices. Based on a typical Williamson-Hall analysis (*23*), we calculated the strain using the full width at half maximum (FWHM) of all the peaks (Fig. 3C and fig. S7). The change from low to high entropy tripled the lattice strains from 0.16 to 0.45%.

Although our XRD analysis showed the macroscopic existence of lattice strains, their type and statistical and spatial distributions were unclear. We used nanobeam electron diffraction (NBED) to detect the lattice strains in a 350-nm–by–350-nm area (*24*) (Fig. 3, D to F, and fig. S8). In these measurements, we used a transmission electron beam with a diameter of 4 nm to measure the lattice parameters and orientations in the beam area. We plotted the normal strain by mapping in two perpendicular directions, [002] and [2-20], which revealed the spatial distribution of the normal strains at the nanoscale (insets of Fig. 3, D and E). We saw that the high-entropy sample had higher strain intensity and stronger strain fluctuation at a scale of around 10 nm, whereas those in the low-entropy sample were much lower and weaker. By counting hundreds of diffraction spots, we plotted frequency histograms (Fig. 3, D and E). The results illustrated the broader strain distribution in the high-entropy sample relative to the low-entropy sample. We conducted similar operations for shear strains along the [2-20] orientation (Fig. 3F) and showed similar large strain fluctuations in the high-entropy sample.

In addition, we further investigated the strain at the atomic scale through STEM-HAADF imaging. We chose a 20-nm–by–20-nm area randomly in both low- and high-entropy samples (fig. S8) and performed geometric phase analysis (GPA) based on STEM-HAADF images to calculate the atomic strains (*25*) (Fig. 3, H and I). We observed that the strain had a short-range strain fluctuation (below 1 nm) because impurity atoms usually affect the nearest and the second nearest atoms (*26*). Similar to the NBED results, the strain distribution fluctuations by GPA in the high-entropy sample were also much larger than those in the low-entropy sample because of the large mass and size differences. The differences in normal strains between low- and high-entropy samples are notably smaller than that of shear strains. This is because normal strains in GPA are calculated from the change of unit cell volume, whereas the shear strains reflect the deformation of the unit cell (*27*). The mismatch of atomic sizes can be easily released by a change of cell volume in low-entropy materials, whereas the atomic off-centering from potential and distribution asymmetry in high-entropy materials were responsible for the deformed unit cell and the large shear strains, which is the key difference between low- and high-entropy materials (*28*). Owing to the asymmetric potential difference and probability distribution functions, the equilibrium positions of atoms in high-entropy material

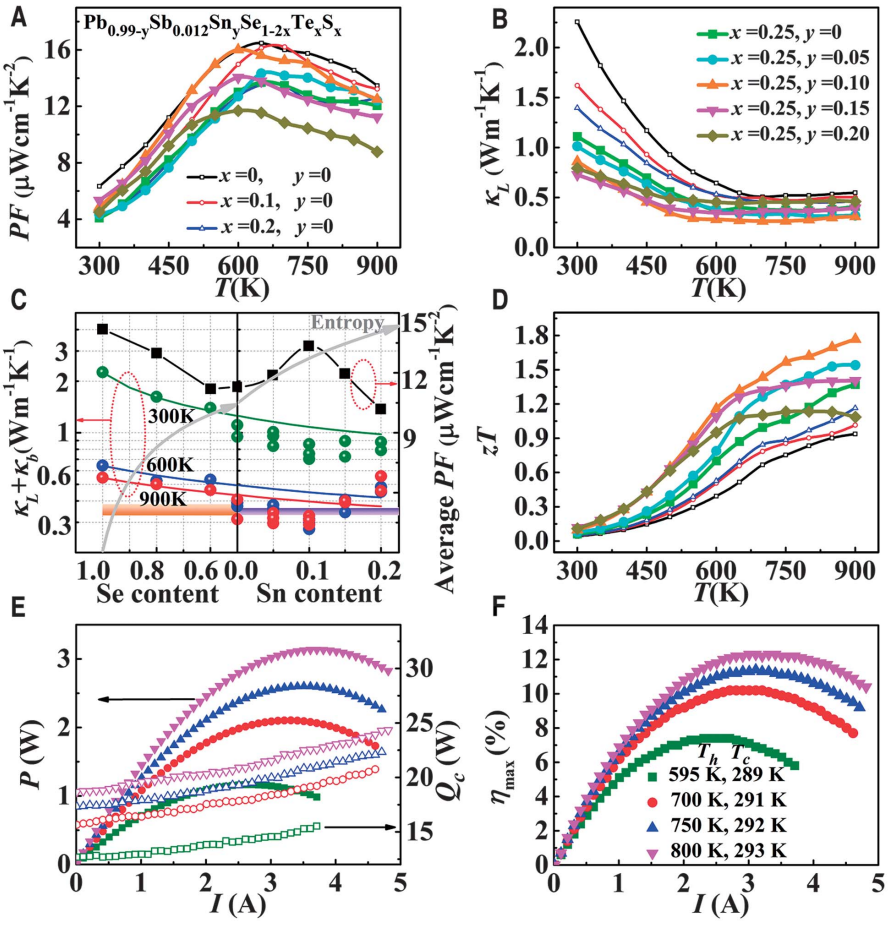

Fig. 4. Thermoelectric properties of $Pb_{0.99-y}Sb_{0.012}Sn_ySe_{1-2x}Te_xS_x$. *x* was changed from 0 to 0.25 and *y* from 0 to 0.2 for the samples. (**A**, **B**, and **D**) Temperature dependences of (A) power factor (*PF*), (B) lattice thermal conductivity ($\kappa_L + \kappa_b$), and (D) *zT* values. κ_b, bipolar thermal conductivity. (**C**) Composition dependence of $\kappa_L + \kappa_b$ and average *PF*. The solid lines are predictions based on the alloy model. The black line represents the experimental average *PF* (right red arrow). The green, blue, and red circles represent experimental lattice thermal conductivity (left red arrow). The orange-purple line represents theoretical minimum lattice thermal conductivity. (**E** and **F**) Shown are (E) output power (*P*, left black arrow) and heat flow at the cold side (Q_c, right black arrow) and (F) maximum conversion efficiency (η_{max}) as a function of the current (*I*) under different operating temperatures for the fabricated segmented thermoelectric module. T_h, temperature at the hot side; T_c, temperature at the cold side.

should deviate from the uniform distribution (figs. S9 to S11). The theoretical lattice strains of high-entropy material (fig. S11) that we calculated showed large shear strains and were consistent with the measured result (Fig. 3).

The entropy-driven structural stabilization and the severely distorted lattice should work together to effect the electrical and thermal transport properties. We measured the thermoelectric properties of n-type Sb-doped (Pb/Sn)(Se/Te/S) materials to evaluate the effect of this high-entropy concept (Fig. 4 and figs. S12 to S14). The electron mobility was well maintained after introducing Sn (fig. S18 and table S3), illustrating that the atomic lattice was well defined even when the system disorder (entropy) was increased. As a result, the power factors of high-entropy samples were well retained owing to the maintained electron mobility. To evaluate the effect of entropy-driven structural stabilization on power factors, we plotted the composition dependence of average power factors for all the samples (Fig. 4C and fig. S15A). The average power factor initially decreased with increasing entropy owing to electron scattering, but the power factor increased when further increasing the entropy because this eliminated phase-boundary electron scattering in the entropy-stabilized structure. The average power factor of 13.4 μW cm^{-1} K^{-2} in the single-phase $Pb_{0.89}Sb_{0.012}Sn_{0.1}Se_{0.5}Te_{0.25}S_{0.25}$ sample is larger than that of 11.2 μW cm^{-1} K^{-2} in the multiphase $Pb_{0.99}Sb_{0.012}Se_{0.5}Te_{0.25}S_{0.25}$ sample, which clearly demonstrates the positive effect of entropy-driven structural stabilization on electrical transport properties. The decreased power factor in the sample with the high Sn content was due to the decreased bandgap rather than high entropy, which resulted in the intrinsic excitation at high temperature (figs. S17 and S18A).The more exciting effect of high entropy was the largely depressed lattice thermal conductivity (κ_L) (Fig. 4B). To make clear the effect of composition and entropy on κ_L, we calculated the composition dependence of κ_L (Fig. 4C). The solid lines were predicted based on a widely accepted alloy model in which the differences in atomic mass and radius were included (table S4) (*29*, *30*). The experimental data for low-entropy samples were consistent with the predicted lines, indicating the suitability of the model. However, the experimental data for the high-entropy samples were lower than the predicted values. The κ_L for the high-entropy sample was largely depressed to an ultralow value of ~0.3 W m^{-1} K^{-1} over a large temperature range (550 to 900 K), which was close to the amorphous limit (*30*, *31*). We

confirmed these results by reproducing the observation on three high-entropy samples (Fig. 4C).

Considering the absence of second phases and nanostructures in high-entropy samples, the similar Grüneisen parameters (table S1), and the high relative densities of all the samples (table S2), the reason for the ultralow κ_L in high-entropy samples should be the large lattice strains distributed at all the scales. The phonon dispersion for a one-dimensional single-atom harmonic chain can be written as (*32*)

$$\omega = 2\sqrt{\frac{F}{M}}\sin\left(\frac{\pi}{2}\frac{k}{k_c}\right)$$

where k, k_c, F, and M are the Boltzmann constant, cut-off wave vector, force constant, and atomic mass, respectively. F and M can be tuned by changing a materials' components, which should result in a fluctuation in phonon dispersion ($\Delta\omega$). Because the lifetime (τ_p) of phonons is proportional to $(\Delta\omega)^{-1}$, the large fluctuation of the force constant (ΔF) and atomic mass (ΔM) should shorten τ_p and depress κ_L, which is written as $\kappa_L \propto \tau_p \propto \frac{1}{\Delta\omega}$ (*33*). In the traditional alloy model, ΔF and ΔM are included to calculate the effect of constituent fluctuations on κ_L (*29*). However, the ΔF from $\Delta r/r_{avg}$, where r is atomic radius, in the model only includes the contribution from the volume variation of the unit cell, called the normal strain (*29*). Therefore, the large fluctuation in the force constant ($\Delta F \propto \varepsilon_{normal} + \varepsilon_{shear}$) from normal and shear strains should result in an ultralow κ_L in high-entropy materials, which is lower than the predicated value that only includes normal strains and is close to the theoretical minimum value (*30*). In addition, a nanoscale strain wave will induce the localization-like behavior of low-frequency phonons, contributing to an ultralow κ_L, as the results show in the superlattice structure and distorted graphene (*34*, *35*).

Owing to the well-maintained high electrical transport properties (*PF*) and the largely depressed κ_L, the zT values can be enhanced from 0.9 to 1.8 at 900 K when the composition changes from n-type low-entropy $Pb_{0.99}Sb_{0.012}Se$ to high-entropy $Pb_{0.89}Sb_{0.012}Sn_{0.1}Se_{0.5}Te_{0.25}S_{0.25}$. Not only was the peak value largely enhanced, but the zT values across the whole temperature range were also tremendously improved, making the average zT increase from 0.45 to 1.02 when the composition changed from low entropy to high entropy (fig. S15B). As of now, because the energy conversion efficiency of lead chalcogenide thermoelectric modules is limited by the low zT value of n-type material (*36*), our enhanced average zT value in n-type PbSe-based material should certainly push forward the applications of thermoelectric modules. Therefore, we used typical p-type Sb-doped Bi_2Te_3, p-type Na-doped PbTe, n-type Se-doped Bi_2Te_3, and our n-type high-entropy PbSe to fabricate a segmented thermoelectric module (fig. S19A). Based on a finite element analysis (*37*), the simulated highest conversion efficiency of our segmented module reached 13.9% at a temperature difference ΔT = 513 K when the ratio of $PbTe/Bi_2Te_3$ and $PbSe/Bi_2Te_3$ was optimized (Fig. 1C). The simulation results and the temperature fields that result from changing the ratio of $PbTe/Bi_2Te_3$ and $PbSe/Bi_2Te_3$ are shown in fig. S19, B to D. We fabricated an eight-couple segmented module (20 mm by 20 mm by 12.5 mm) with a ratio of 2.6 (inset of Fig. 1C) and measured its output properties (Fig. 4, E and F, and fig. S20). At ΔT = 507 K and current I = 3.7 A, we measured the internal resistance as 230 milliohms and the power output (P) reached a maximum value of 3.1 W. By measuring the heat flow on the cold side (Fig. 4E) (*37*), the maximum conversion efficiency (η_{max}) reached 12.3%. The deviation of experimental data from simulated data was from the contact resistance of interfaces and the heat emissivity of radiative heat flow. Thus, further improvements could be achieved by optimizing the contact interface and geometrical configuration.

We demonstrate that different high-entropy thermoelectric materials can be formed by entropy-driven structural stabilization, with electrical transport properties that are well maintained by the stabilized structure. Meanwhile, the large strains from the severely distorted lattice in this high-entropy material provide strong scattering for heat-carrying phonons, contributing to an ultralow κ_L. As a consequence, a high zT value (1.8 at 900 K, n-type) and conversion efficiency (12.3% at ΔT = 507 K) in the high-entropy material and module were realized in the experiments. Our demonstration provides insight into entropy engineering for high-performance thermoelectric materials and modules, which we expect to be an attractive pathway for developing high-performance functional materials.

REFERENCES AND NOTES

1. J. Mao *et al.*, *Science* **365**, 495–498 (2019).
2. G. Tan, L. D. Zhao, M. G. Kanatzidis, *Chem. Rev.* **116**, 12123–12149 (2016).
3. J. He, T. M. Tritt, *Science* **357**, eaak9997 (2017).
4. G. J. Snyder, E. S. Toberer, *Nat. Mater.* **7**, 105–114 (2008).
5. C. Chang *et al.*, *Science* **360**, 778–783 (2018).
6. Y. Pei *et al.*, *Nature* **473**, 66–69 (2011).
7. J. P. Heremans, B. Wiendlocha, A. M. Chamoire, *Energy Environ. Sci.* **5**, 5510–5530 (2012).
8. B. Poudel *et al.*, *Science* **320**, 634–638 (2008).
9. H. Liu *et al.*, *Nat. Mater.* **11**, 422–425 (2012).
10. N. Dragoe, D. Bérardan, *Science* **366**, 573–574 (2019).
11. J. W. Yeh *et al.*, *Adv. Eng. Mater.* **6**, 299–303 (2004).
12. C. M. Rost *et al.*, *Nat. Commun.* **6**, 8485 (2015).
13. A. Sarkar *et al.*, *Adv. Mater.* **31**, e1806236 (2019).
14. L. Hu *et al.*, *Adv. Energy Mater.* **8**, 1802116 (2018).
15. J. L. Braun *et al.*, *Adv. Mater.* **30**, e1805004 (2018).
16. C. M. Rost *et al.*, *Acta Mater.* **196**, 231–239 (2020).
17. D. Bérardan, A. K. Meena, S. Franger, C. Herrero, N. Dragoe, *J. Alloys Compd.* **704**, 693–700 (2017).
18. R. Liu *et al.*, *Adv. Mater.* **29**, 1702712 (2017).
19. B. Jiang *et al.*, *J. Mater. Chem. C* **5**, 943–952 (2017).
20. B. Jiang *et al.*, *Mater. Today Phys.* **5**, 20–28 (2018).
21. R. J. Korkosz *et al.*, *J. Am. Chem. Soc.* **136**, 3225–3237 (2014).
22. D. B. Miracle, O. N. Senkov, *Acta Mater.* **122**, 448–511 (2017).
23. G. K. Williamson, W. H. Hall, *Acta Metall.* **1**, 22–31 (1953).
24. A. Béché, J. L. Rouvière, J. P. Barnes, D. Cooper, *Ultramicroscopy* **131**, 10–23 (2013).
25. F. Hüe, M. Hÿtch, H. Bender, F. Houdellier, A. Claverie, *Phys. Rev. Lett.* **100**, 156602 (2008).
26. P. M. Fahey, P. B. Griffin, J. D. Plummer, *Rev. Mod. Phys.* **61**, 289–384 (1989).
27. A. L. Greer, Y. Q. Cheng, E. Ma, *Mater. Sci. Eng. Rep.* **74**, 71–132 (2013).
28. H. Song *et al.*, *Phys. Rev. Mater.* **1**, 023404 (2017).
29. J. Yang, G. P. Meisner, L. Chen, *Appl. Phys. Lett.* **85**, 1140–1142 (2004).
30. D. G. Cahill, S. K. Watson, R. O. Pohl, *Phys. Rev. B* **46**, 6131–6140 (1992).
31. L. D. Zhao *et al.*, *Appl. Phys. Lett.* **97**, 092118 (2010).
32. Y. Wu *et al.*, *Joule* **3**, 1276–1288 (2019).
33. E. Bouchbinder, E. Lerner, *New J. Phys.* **20**, 073022 (2018).
34. R. Venkatasubramanian, *Phys. Rev. B* **61**, 3091–3097 (2000).
35. L. Cui, X. Du, G. Wei, Y. Feng, *J. Phys. Chem. C* **120**, 23807–23812 (2016).
36. Y. Xiao *et al.*, *J. Am. Chem. Soc.* **139**, 18732–18738 (2017).
37. Q. Zhang *et al.*, *Energy Environ. Sci.* **10**, 956–963 (2017).
38. H. Wang, Y. Pei, A. D. LaLonde, G. J. Snyder, *Proc. Natl. Acad. Sci. U.S.A.* **109**, 9705–9709 (2012).
39. Q. Zhang *et al.*, *Energy Environ. Sci.* **5**, 5246–5251 (2012).
40. Z. Luo *et al.*, *Energy Environ. Sci.* **11**, 3220–3230 (2018).
41. Z. Chen *et al.*, *Nat. Commun.* **8**, 13828 (2017).
42. J. Androulakis *et al.*, *J. Am. Chem. Soc.* **133**, 10920–10927 (2011).
43. A. Singh *et al.*, *J. Phys. D Appl. Phys.* **42**, 015502 (2009).
44. P. Jood, M. Ohta, A. Yamamoto, M. G. Kanatzidis, *Joule* **2**, 1339–1355 (2018).
45. X. Hu *et al.*, *Energy Environ. Sci.* **9**, 517–529 (2016).
46. J. D'Angelo *et al.*, *J. Electron. Mater.* **40**, 2051–2062 (2011).
47. B. Jiang *et al.*, *Energy Environ. Sci.* **13**, 579–591 (2020).
48. D. Zhao *et al.*, *Mater. Sci. Semicond. Process.* **13**, 221–224 (2010).
49. P. Zong *et al.*, *Energy Environ. Sci.* **10**, 183–191 (2017).
50. Q. Zhang *et al.*, *Nano Energy* **41**, 501–510 (2017).
51. C. Fu *et al.*, *Nat. Commun.* **6**, 8144 (2015).
52. Y. Xing *et al.*, *Energy Environ. Sci.* **12**, 3390–3399 (2019).

ACKNOWLEDGMENTS

Funding: We acknowledge support from the leading talents of the Guangdong Province Program (grant no. 00201517), the Guangdong-Hong Kong-Macao Joint Laboratory (grant no. 2019B121205001), the National Natural Science Foundation of China (grant nos. 52002167, 11874194, 11934007, and 51632005), the Science and Technology Innovation Committee Foundation of Shenzhen (grant nos. KQTD20160226195659 91 and ZDSYS20141118160434515), and a high level of special funds (G02206302). L.C. is grateful for support from the National Natural Science Foundation of China (grant no. 51632010).
Author contributions: Bi.J. and J.H. designed this work. Bi.J. synthesized the samples and carried out the transport property measurements. Y.Y., L.X., Y.H., and S.N. performed the transmission electron microscopy observations and analysis. J.C. performed the calculations. Bi.J., X.L., J.L., Q.Z., Ba.J., and B.Z. carried out the study on module fabrication and characterization. S.B., L.C., S.J.P., and J.H. analyzed the experimental data. Bi.J., Y.Y., J.C., and J.H. wrote and all authors edited this manuscript. **Competing interests:** None declared.
Data and materials availability: All data are available in the manuscript and supplementary materials.

SUPPLEMENTARY MATERIALS

science.sciencemag.org/content/371/6531/830/suppl/DC1
Materials and Methods
Supplementary Text
Figs. S1 to S20
Tables S1 to S4
References (*53*–*66*)

1 August 2020; accepted 18 January 2021
10.1126/science.abe1292

High-entropy-stabilized chalcogenides with high thermoelectric performance

Binbin Jiang, Yong Yu, Juan Cui, Xixi Liu, Lin Xie, Jincheng Liao, Qihao Zhang, Yi Huang, Shoucong Ning, Baohai Jia, Bin Zhu, Shengqiang Bai, Lidong Chen, Stephen J. Pennycook and Jiaqing He

Science **371** (6531), 830-834.
DOI: 10.1126/science.abe1292

Distorted thermal properties

Thermoelectric devices can convert waste heat into electricity, providing one path for improving energy efficiency. Jiang *et al.* leveraged entropy engineering to synthesize a single-phase high-entropy alloy with attractive thermoelectric properties. By increasing the number of elements in the alloy, the resulting disorder helps to stabilize against breakdown into multiple phases. The disordered and distorted crystal lattice suppresses thermal transport while maintaining the electrical properties, which boosts the heat-conversion efficiency of the material.

Science, this issue p. 830